

Using local nuclear scaling of initial condition parameters to improve the system size dependence of transport model descriptions of nuclear collisions

Chao Zhang,^{1,2} Liang Zheng,³ Shusu Shi,¹ and Zi-Wei Lin^{2,*}

¹*Key Laboratory of Quark and Lepton Physics (MOE) and Institute of Particle Physics, Central China Normal University, Wuhan 430079, China*

²*Department of Physics, East Carolina University, Greenville, North Carolina 27858, USA*

³*School of Mathematics and Physics, China University of Geosciences (Wuhan), Wuhan 430074, China*

We extensively study the system size dependence of nuclear collisions with a multi-phase transport model. Previously certain key parameters for the initial condition needed significantly different values for pp and central AA collisions for the model to reasonably describe the yields and transverse momentum spectra of the bulk matter in those collision systems. Here we scale two key parameters, the Lund string fragmentation parameter b_L and the minijet transverse momentum cutoff p_0 , with local nuclear thickness functions from the two colliding nuclei. This allows the model to use the parameter values for pp collisions with the local nuclear scaling to describe the system size and centrality dependences of nuclear collisions self consistently. In addition to providing good descriptions of pp collisions from 23.6 GeV to 13 TeV and reasonable descriptions of the centrality dependence of charged particle yields for Au+Au collisions from 7.7A GeV to 200A GeV and Pb+Pb collisions at LHC energies, the improved model can now well describe the centrality dependence of the mean transverse momentum of charged particles below $p_T \lesssim 2$ GeV. It works similarly well for smaller systems including p Pb, Cu+Cu and Xe+Xe collisions.

I. INTRODUCTION

A main purpose of the field of high energy heavy ion collisions is to explore the properties of the produced hot and dense matter, the quark-gluon plasma (QGP). Many theoretical models including transport models [1–4], hydrodynamic models [5–8], and hybrid models [9–11] are constructed to simulate and study the phase space evolution of the QGP. Comprehensive comparisons between such models and the experimental data can provide us key information of the high density matter.

In particular, the dependences of various observables on the size of the collision system or the centrality of a given collision system are useful as they may exhibit the onset or transition of certain phenomena such as the momentum anisotropy from initial state correlations [12, 13] or from final state interactions [14–18]. For large systems, it is commonly believed that viscous hydrodynamics applies well to the bulk of the matter, while transport model essentially approach the hydrodynamical limit since the average number of collisions per parton is large. For small colliding systems, however, hydrodynamic models and transport models may be quite different due to non equilibrium dynamics. Recently it has been found that parton transport can convert the initial spatial anisotropy into significant anisotropic flows in the momentum space through the parton escape mechanism [14, 15], especially in small systems where the average number of collisions per particle is relatively small. Studies [17] also show that transport theory with a single scattering is very efficient in changing the particle distribution. Therefore, the system size dependence of anisotropic flows could pro-

vide key information on the origin of collectivity and the region of applicability of hydrodynamics in nuclear collisions.

A multi-phase transport (AMPT) model, which we improve in this study, contains four main parts: the fluctuating initial condition from the HIJING model [19], partonic interactions, hadronization, and hadronic interactions. The string melting version of AMPT model can reasonably describe many experimental data at low p_T in central and semi-central Au+Au collisions at 200A GeV and Pb+Pb collisions at the LHC [20, 21] including the pion, kaon, proton yields, p_T spectra and elliptic flow. Recently we updated the AMPT model with a new quark coalescence model [21] and modern nuclear parton distribution functions (nPDFs) [22], where the string melting version can also reasonably describe the charged particle rapidity distributions and p_T spectra in pp collisions at different energies. On the other hand, from the comparison to experimental data we have found that certain key parameters in the AMPT model need to have very different values for pp and central AA collisions. First, the b parameter in the Lund symmetric fragmentation function [23, 24] (denoted as b_L in this study) needs to be $\approx 0.15/\text{GeV}^{-2}$ for central Au+Au or Pb+Pb collisions, which is a few times smaller than its value for pp collisions. Second, the minijet transverse momentum cutoff p_0 for central Pb+Pb collisions at the LHC energies needs to be significantly bigger than its value for pp collisions at the same energy in the AMPT model updated with modern nPDFs [22]. These observations clearly indicate that these two parameters should depend on the size of the colliding system.

In this study we improve the system size and centrality dependences of the AMPT model [3] by treating the two parameters in its initial condition, the Lund b_L parameter and the minijet cutoff p_0 , as local variables that

* linz@ecu.edu

depend on the local nuclear thickness functions, $T_A(s_A)$ and $T_B(s_B)$, from the two colliding nuclei in each event. The rest of the paper is organized as follows. In Sec. II we discuss the local nuclear scaling of the Lund b_L and momentum cutoff p_0 parameters. We then systematically compare results from the improved AMPT model with the experimental data for pp , pA , and AA collisions at RHIC and LHC energies in Sec. III, including the charged particle yields and p_T spectrum or mean p_T and their centrality dependences in nuclear collisions. After more discussions in Sec. IV, we then summarize in Sec. V.

II. IMPROVEMENT OF THE INITIAL CONDITION OF THE AMPT MODEL

The initial condition component of the AMPT model is based on the HIJING two component model [19]. The primary interactions between the two incoming nuclei are divided into two components: the soft component described by the Lund string fragmentation model [23–25] that includes the parameter b_L , and the hard component with a minijet transverse momentum cutoff p_0 that is described by perturbative QCD through the PYTHIA program [25]. Rather than treating p_0 and b_L as constant parameters (at least for a given collision system at a given energy), as done in almost all previous studies with the AMPT model, here we model them as local variables that depend on the nuclear thickness functions of the two nuclei.

A. Local Lund string fragmentation parameter b_L

In the Lund string model [23, 24], the symmetric fragmentation function is given by

$$f(z) \propto z^{-1}(1-z)^{a_L} e^{-b_L m_T^2/z}, \quad (1)$$

where z is the light-cone momentum fraction of the produced hadron with respect to the fragmenting string, and m_T is the hadron transverse mass. The average squared transverse momentum of massless hadrons from fragmentation is then related to the Lund fragmentation parameters a_L and b_L as [3]

$$\langle p_T^2 \rangle = \frac{1}{b_L(2+a_L)}. \quad (2)$$

As a result, the average p_T of partons after string melting and consequently the final hadron p_T spectrum from the string melting version of the AMPT model strongly depend on b_L . In the AMPT model updated with modern nPDFs [22], we have found that a constant values of $a_L = 0.8$ and $b_L = 0.4 \text{ GeV}^{-2}$ can reasonably describe the p_T spectra of pp and $p\bar{p}$ collisions over a wide energy range. However, a much smaller value of $b_L \approx 0.15 \text{ GeV}^{-2}$ is needed to describe the p_T spectra in central Au+Au collisions at RHIC and central Pb+Pb collisions

at LHC [20–22]. It was also realized that the centrality dependence of the charged particle mean transverse momentum $\langle p_T \rangle$ in heavy ion collisions has the opposite trend in comparison to the experimental data [26], where the system size dependence of the Lund fragmentation parameters was proposed as a possible solution. Since we expect the mean transverse momentum of initial partons to be higher in larger systems due to the higher initial temperature and Eq.(2) relates the mean squared transverse momentum after string melting to the Lund b_L parameter, it is natural that b_L should depend on the system size.

We now make b_L a local variable that depends on the transverse position of the corresponding excited string in each event. Note that its value has been found to be smaller for a larger collision system, which is consistent with the expectation of a stronger color field and thus a higher string tension κ since $\kappa \propto 1/b_L$ [3]. Therefore we scale b_L with the local nuclear thickness functions in a general AB collision as

$$b_L(s_A, s_B, s) = \frac{b_L^{pp}}{\left[\sqrt{T_A(s_A)T_B(s_B)}/T_p\right]^{\beta(s)}}. \quad (3)$$

In the above, b_L^{pp} is the value for pp collisions (to be discussed further in Sec. III A), s is the square of the center-of-mass collision energy per nucleon pair, $T_A(s_A) = \int \rho_A(s_A, z)dz$ is the nuclear thickness function at the transverse distance s_A from the center of nucleus A from Woods-Saxon nuclear density profiles [27], and T_p (taking the value of 0.22 fm^{-2} in this study) can be considered as the average value of the effective thickness function of the proton. Note that in Eq.(3) (and Eqs. (7), (9) and (10)) T_p is used instead of $T_A(s_A)$ or $T_B(s_B)$ when the projectile or the target is proton or when $T_A(s_A)$ or $T_B(s_B)$ from the nucleus is smaller than the T_p value. Also note that there are two types of strings in the fragmentation process. The first type is a wounded nucleon from the projectile (or target) nucleus that has interacted with one or more nucleons in the target (or projectile); we take the nucleon position in the nucleus s_A (or s_B) in Eq.(3) and then for simplicity take the other position s_B (or s_A) via the relation $\vec{s}_B = \vec{s}_A + \vec{b}$. The other type is an independent string from the primary nucleon-nucleon interaction through the hard process, where the values of both s_A and s_B are unique and thus directly used in Eq.(3).

First we have determined that a constant value $b_L^{pp} = 0.7 \text{ GeV}^{-2}$ provides a reasonably good description of the charged particle $\langle p_T \rangle$ in pp collisions (details in Sec.III A). Next we fit the charged particle $\langle p_T \rangle$ in the most central Au+Au collisions at RHIC energies and most central Pb+Pb collisions at LHC energies to obtain the preferred $\beta(s)$ value at each of those energies. The results show that the preferred $\beta(s)$ is almost a constant at RHIC energies but needs to be significantly bigger at LHC en-

ergies. We thus parametrize the $\beta(s)$ function as

$$\beta(s) = 0.620 + 0.112 \ln \left(\frac{\sqrt{s}}{E_0} \right) \Theta(\sqrt{s} - E_0), \quad (4)$$

where $E_0 = 200$ GeV, \sqrt{s} is the center-of-mass collision energy per nucleon pair, and $\Theta(x)$ is the theta function. The fitted $\beta(s)$ function is shown in Fig. 1(a) (dashed line). Note that the fit is not constrained or tested by data between the energy of $200A$ GeV and $2.76A$ TeV or above $5.44A$ TeV due to the lack of heavy ion data. On the other hand, the value of $\beta = 1$ (dotted line) may be a “natural” limit for Eq.(3) at high energies if all local strings would fully overlap so that the string tension would add up, since it corresponds to $b_L \propto 1/T_A(s_A)$ for central AA collisions where $T_A(s_A)$ is proportional to the local number of participant nucleons or excited strings integrated over the longitudinal length.

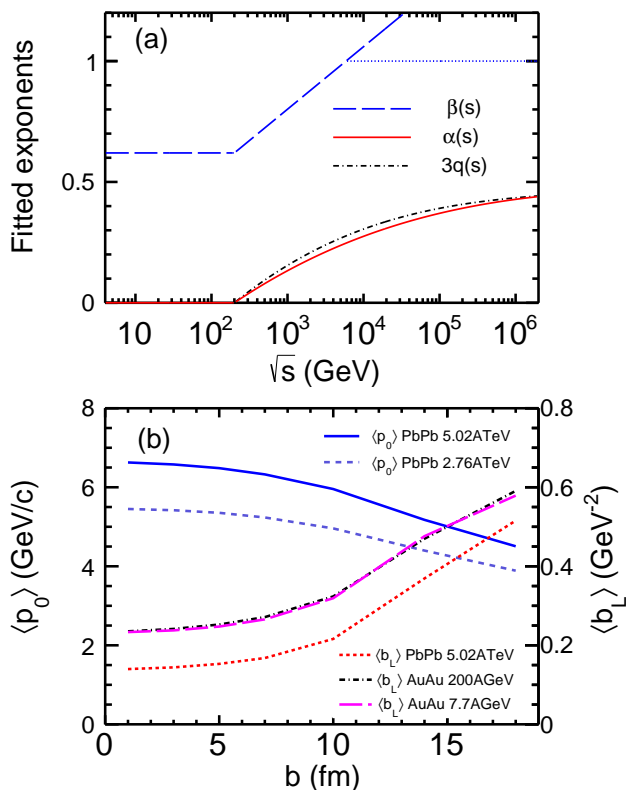


FIG. 1. (a) Fitted exponent functions $\beta(s)$ and $\alpha(s)$ versus the center-of-mass energy per nucleon pair \sqrt{s} , where the function $3q(s)$ is also shown for comparison. (b) Average p_0 and b_L values versus the impact parameter in Pb+Pb and Au+Au collisions at several energies.

Figures 2(a) and 2(b) show the distributions of b_L values of Eq.(3) over the transverse plane of multiple central ($b = 0$) and peripheral ($b = 10$ fm) 5.02A TeV Pb+Pb events, respectively, from the AMPT model simulations. Specifically, each point represents the b_L value

of a wounded nucleon or an independent string versus its transverse position in the collision. The red and black circles represent the hard-sphere boundaries of the projectile and target nuclei, respectively, to indicate the scale. We see that the values in less-overlapped regions are close to the value for pp collisions, while the b_L values in highly-overlapped regions are much lower. Figure 1(b) shows the b_L value averaged over the overlap volume as a function of the impact parameter for Pb+Pb collisions at 5.02A TeV and Au+Au collisions at two RHIC energies. We see that as expected $\langle b_L \rangle$ at the LHC energy is lower due to the larger value of the exponent $\beta(s)$, while the impact parameter dependences of $\langle b_L \rangle$ at different RHIC energies are essentially the same due to the constant value of $\beta(s)$ within that energy range.

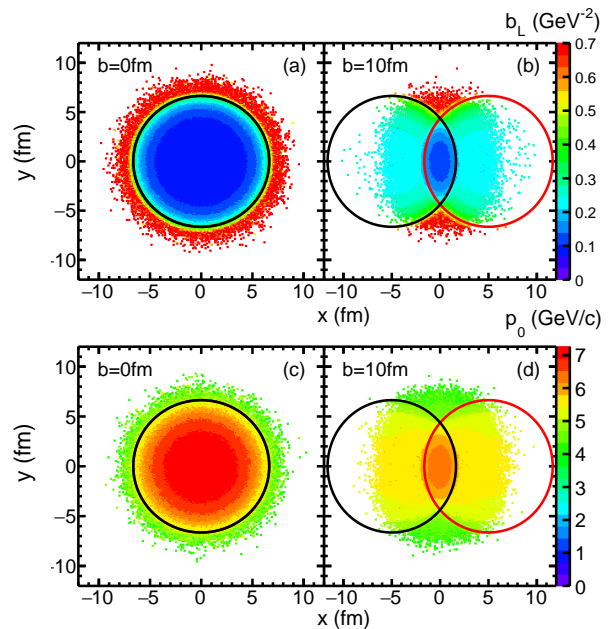


FIG. 2. Distributions of b_L values of Eq.(3) (upper panels) and p_0 values of Eq.(7) (lower panels) over the transverse plane from multiple central (left panels) and peripheral (right panels) Pb+Pb events at 5.02A TeV from the AMPT model.

B. Local minijet transverse momentum cutoff p_0

In the hard component of the HIJING model, the total jet cross section is given by

$$\sigma_{\text{jet}} = \sum_{c,d} \frac{1}{1 + \delta_{cd}} \int dy_1 dy_2 \int_{p_0^2}^{\hat{s}/4} dp_T^2 \frac{d\sigma^{cd}}{dp_T^2 dy_1 dy_2}. \quad (5)$$

In the above, p_0 is the cutoff of the minijet transverse momentum, \hat{s} is the Mandelstam variable for the minijet production subprocess, and $d\sigma^{cd}/(dp_T^2 dy_1 dy_2)$ is the differential cross section [28] for the two colliding nuclei to produce the pair of minijet partons of flavor c and d

at rapidity y_1 and y_2 , respectively. The p_0 cutoff (relevant when $\sqrt{s} > 10$ GeV) together with the soft component cross section (σ_{soft}) are the two key parameters to determine the total, elastic and inelastic cross sections of nuclear collisions in the HIJING model [19, 22, 29]. In our recent update of the AMPT model with modern nPDFs [22], using the pp cross section data we determined p_0 and σ_{soft} as functions of the colliding energy. Motivated by the physics of color glass condensate [30], we further introduced a nuclear scaling of the p_0 cutoff for central AA collisions above the top RHIC energy of 200A GeV to describe the experimental data on charged particle yields in central Pb+Pb collisions at LHC energies. That scaling [22] can be considered as a global nuclear scaling because the scaled p_0 value is a constant for all events of a given collision system at a given energy.

In a subsequent work that improved heavy flavor productions [31], we started to use the minijet cross section as shown in Eq.(5), which changed the factor of 1/2 in the original HIJING model [3, 19, 22] to $1/(1 + \delta_{cd})$ to differentiate minijet final states with or without identical partons. We also removed the momentum cutoff for heavy quark productions and then included heavy quark production cross sections in the total minijet cross section [31]. These modifications have little effect on σ_{soft} , but they lead to an increase of the total minijet cross section and consequently a small increase of the p_0 cutoff in pp collisions as given below:

$$p_0^{pp}(s) = -1.92 + 1.77 \ln(\sqrt{s}) - 0.274 \ln^2(\sqrt{s}) + 0.0176 \ln^3(\sqrt{s}) \quad (6)$$

with \sqrt{s} in GeV. For the global nuclear scaling relation $p_0^{AA}(s) = p_0^{pp}(s)A^{q(s)}$ [31], the modifications also lead to a small change of the nuclear scaling exponent $q(s)$ for central AA collisions: $q(s) = 0.0369 \ln(\sqrt{s}/E_0) - 0.00318 \ln^2(\sqrt{s}/E_0) + 0.0000990 \ln^3(\sqrt{s}/E_0)$ for $\sqrt{s} \geq E_0$ while $q(s) = 0$ for $\sqrt{s} < E_0$. On the other hand, we do not expect the global nuclear scaling to hold for non-central AA collisions; for example, we expect little nuclear scaling for very peripheral AA collisions since they should be similar to pp collisions. Indeed, we have shown [22] that the charged particle yield in peripheral Pb+Pb collisions at 5.02A TeV is better described without using the global nuclear scaling of p_0 , although the scaling is necessary for central Pb+Pb collisions.

We now go beyond the global nuclear scaling and instead make p_0 a local variable that depends on the transverse position of the corresponding hard process in each event. Since the p_0 cutoff has been found to increase with the system size, it is natural to relate it to the nuclear thickness functions in a general AB collision; thus we write

$$p_0(s_A, s_B, s) = p_0^{pp}(s) * \left[\sqrt{T_A(s_A)T_B(s_B)}/T_p \right]^{\alpha(s)}. \quad (7)$$

Since $T_A(s_A) \propto A^{1/3}$, Eq.(7) approximately gives $p_0 \propto A^{\alpha(s)/3}$ for central AA collisions and thus essentially

recovers the previous global nuclear scaling relation if $\alpha(s) = 3q(s)$. On the other hand, for peripheral collisions $T_A(s_A)$ and $T_B(s_B)$ are expected to be small and close to the proton value (T_p), then Eq.(7) automatically gives the p_0 value for pp collisions. This way Eq.(7) captures the expected system size dependence as well the centrality dependence of the p_0 cutoff parameter.

From the comparison to charged particle yields in the most central Pb+Pb collisions at 2.76A TeV and 5.02A TeV, we obtain the preferred $\alpha(s)$ values at those two energies. Since $p_0^{pp}(s)$ works for central Au+Au collisions at 200A GeV, we assume that the need to modify p_0 in nuclear collisions starts at the top RHIC energy [22]. We then fit the $\alpha(s)$ function as

$$\alpha(s) = 0.0918 \ln\left(\frac{\sqrt{s}}{E_0}\right) - 0.00602 \ln^2\left(\frac{\sqrt{s}}{E_0}\right) + 0.000134 \ln^3\left(\frac{\sqrt{s}}{E_0}\right), \text{ for } \sqrt{s} \geq E_0 \quad (8)$$

with $\alpha(s) = 0$ for $\sqrt{s} < E_0$. As shown in Fig. 1(a), $\alpha(s) \approx 3q(s)$ as expected, and both have values close to 1/2 at the very high energy of 10^8 GeV. Note that the high energy $q(s)$ value of about 1/6 [22] is motivated by the color glass condensate [30], where the saturation momentum Q_s scales with the nuclear size as $Q_s \propto A^{1/6}$ in the saturation regime.

Figures 2(c) and 2(d) show the distributions of p_0 values of Eq.(7) over the transverse plane of multiple central ($b = 0$) and peripheral ($b = 10$ fm) simulated 5.02A TeV Pb+Pb events, respectively. Each point represents the p_0 value of a wounded nucleon that is involved in hard processes versus its transverse position in the collision. Similar to Figs. 2(a) and 2(b), we see that the p_0 value varies from p_0^{pp} (≈ 4.2 GeV at this energy) in less-overlapped regions to bigger values in highly-overlapped regions as expected, and the variation is larger for more central collisions. In addition, the relative variation of the p_0 values is much smaller than that of the b_L values because $\alpha(s) \ll \beta(s)$ for the exponents. The average p_0 value, i.e., averaged over the wounded nucleons in the overlap volume, is shown in Fig. 1(b) as a function of the impact parameter for Pb+Pb collisions at 2.76A TeV and 5.02A TeV. We see that $\langle p_0 \rangle$ gradually decreases with the increase of impact parameter and that $\langle p_0 \rangle$ is smaller at the lower LHC energy due to the smaller $\alpha(s)$ value there.

III. RESULTS FOR VARIOUS COLLISION SYSTEMS

We apply the local Lund parameter b_L of Eq.(3) and local minijet cutoff p_0 of Eq.(7) to systematically study charged particle productions in different collision systems over a wide range of energies.

A. pp and $p\bar{p}$ collisions

For pp and $p\bar{p}$ collisions we first determine the value of b_L^{pp} in Eq.(3), while the minijet cutoff $p_0^{pp}(s)$ has been specified in Eq.(6). We first obtain the preferred value of b_L at each energy (symbols in Fig. 3) by fitting the mean p_T data of charged particles in pp or $p\bar{p}$ collisions from 23.6 GeV to 13 TeV ($p\bar{p}$ at 546, 900, and 1800 GeV). The uncertainty of b_L at each energy is obtained by assuming a 3% uncertainty for the experimental $\langle p_T \rangle$ value. We see that the preferred central value of b_L fluctuates approximately within $[0.4-1.0]$ GeV^{-2} and a constant value of 0.7 GeV^{-2} (dashed line) describes the experimental $\langle p_T \rangle$ data within about 3%. Therefore we take $b_L^{pp} = 0.7 \text{ GeV}^{-2}$ for pp and $p\bar{p}$ collisions at all energies. Note that a constant Lund parameter $a_L = 0.8$ is taken for all collision systems at all energies in the AMPT model improved with modern nPDFs [22, 31].

The $\langle p_T \rangle$ in this study is calculated for charged hadrons up to $p_T \approx 2 \text{ GeV}/c$ for both the AMPT results and the experimental data, because the AMPT model cannot reliably be used for high p_T hadrons due to its lack of the radiative energy loss and independent fragmentation of high p_T partons. Note the different p_T ranges used for the $\langle p_T \rangle$ calculation in Fig. 3: $[0.90, 2.15]$ GeV/c at 23.6 GeV [32], $[0.73, 2.10]$ GeV/c at 53 GeV [32], $[0.6, 2]$ GeV/c at 62.4 GeV [33], $[0.2, 2]$ GeV/c at 200 GeV [34], 546 GeV and 900 GeV [35], $[0.1, 2]$ GeV/c at 2.36 TeV [36], and $[0.15, 2]$ GeV/c at 1.8 TeV [37], 2.76 TeV [38], 5.02 TeV [39], 7 TeV [40] and 13 TeV [41]. Also note that in this study we treat charged particles from the AMPT model more carefully in the comparisons with data. Specifically, we decay the Σ^+, Σ^- hyperons including their antiparticles as well as all open charm hadrons (with PYTHIA [42]) before calculating charged particle observables. This treatment leads to a slight increase of the charged particle yield at low p_T but a slight decrease at high p_T (by several percent) compared to results using the previous analysis method [22].

Figures 4(a) and 4(b) show respectively the $dN_{ch}/d\eta$ distributions and the p_T spectra around mid-pseudorapidity of charged particles from the string melting AMPT model (curves) in comparison with the experimental data (symbols) in pp or $p\bar{p}$ collisions over a wide energy range. We see that using the constant Lund fragmentation parameters $a_L = 0.8$ and $b_L^{pp} = 0.7 \text{ GeV}^{-2}$ allows us to reasonably describe these data.

In the $dN_{ch}/d\eta$ distribution we use the same procedure to select the events from the AMPT model calculations as the experimental data. The ISR data are for inelastic pp collisions [32]. The ALICE non-single-diffractive (NSD) data [41, 43] refer to events that have at least one charged particle on each side of the V0 detectors which cover the η range of $2.8 < \eta < 5.1$ and $-3.7 < \eta < -1.7$, while for the UA5 [44], CDF [37] and CMS [40] data the detectors cover the range of $2 < |\eta| < 5.6$, $3.2 < |\eta| < 5.9$ and $2.9 < |\eta| < 5.2$, respectively. For the transverse momentum spectra, we use the same η cut as the ex-

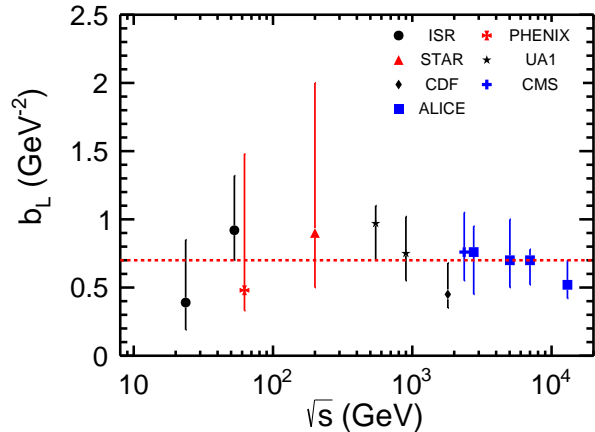


FIG. 3. The preferred individual b_L values from fitting the experimental $\langle p_T \rangle$ of charged particles in pp or $p\bar{p}$ collisions at different energies; the error bar corresponds to an assumed 3% uncertainty of the experimental $\langle p_T \rangle$ value, while the dashed line represents our choice of $b_L^{pp} = 0.7 \text{ GeV}^{-2}$ in this study.

perimental data: $|\eta| < 0.35$ for pp collisions at 23.6 and 53 GeV [32, 45], $|\eta| < 2.5$ for $p\bar{p}$ collisions at 200, 546 and 900 GeV [35], $|\eta| < 1$ for $p\bar{p}$ collisions at 1.8 TeV [46], $0 < \eta < 0.2$ for pp collisions at 2.36 TeV [36], and $|\eta| < 0.8$ for pp collisions at 5.02 [39], 7 and 13 TeV [41]. Also, the event selection procedure is the same as that used for Fig. 4(a), while the UA1 [35] selection criterion is the same as UA5. For the experimental data at LHC energies shown in Fig. 4(b), we have converted the Ed^3N/dp^3 data and AMPT Ed^3N/dp^3 results to $Ed^3\sigma/dp^3$ with the multiplication factor σ_{inel} . Note that the b_L^{pp} value of 0.7 GeV^{-2} here is different than the earlier value of 0.4 GeV^{-2} [22] mostly because we now determine its value from a systematic fit to the $\langle p_T \rangle$ data. We also need to point out that in the earlier study [22] the AMPT results on the invariant transverse momentum cross sections for the lowest two energies (23.6 and 53 GeV) were mistakenly divided by a factor of two.

B. Au+Au and Pb+Pb collisions

We now apply the improved AMPT model to Au+Au and Pb+Pb collisions. Figures 5(a) and 5(b) show respectively the $dN_{ch}/d\eta$ yield at mid-pseudorapidity and mean transverse momentum $\langle p_T \rangle$ around mid-rapidity of charged particles from the AMPT model versus centrality in comparison with experimental data for Au+Au collisions at RHIC energies and Pb+Pb collisions at LHC energies. We use the same method to determine centrality as the experiments. For example, the centrality for the LHC results (from the ALICE Collaboration) is based on the multiplicity of charged particles within $2.8 < \eta < 5.1$ and $-3.7 < \eta < -1.7$, while for the PHENIX, PHOBOS and STAR experiments at RHIC energies the central-

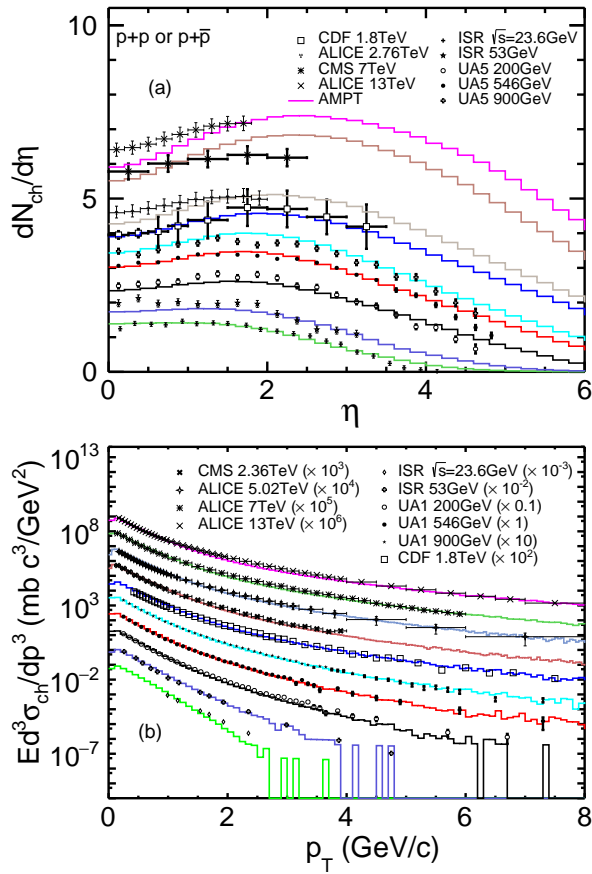


FIG. 4. (a) Pseudorapidity distributions of charged particles in inelastic pp collisions at 23.6 and 53 GeV, NSD $p\bar{p}$ collisions at 200, 546, 900 and 1800 GeV, and NSD pp collisions at 2.76, 7 and 13 TeV from the AMPT model in comparison with the experimental data. (b) Invariant transverse momentum cross sections around mid-pseudorapidity from the AMPT model in comparison with the experimental data that also include pp collisions at 2.36 TeV.

ity is based on the charged particle multiplicity within $3.0 < |\eta| < 3.9$, $|\eta| < 3.2$, and $|\eta| < 0.5$, respectively. Note that the $\langle p_T \rangle$ values from both the AMPT model and experimental data correspond to charged particles within the p_T range of $[0.4, 1.3]$ GeV/c for collision energies from 7.7A to 39A GeV [47], $[0.2, 2]$ GeV/c at 62.4A [48] and 200A GeV [34], and $[0.15, 2]$ GeV/c at 2.76A [49] and 5.02A TeV [39]. Also, results in Fig. 5(b) correspond to the (pseudo)rapidity range of $|y| \leq 0.1$ at energies from 7.7A to 39A GeV, $0.2 < \eta < 1.4$ at 62.4A GeV, $|\eta| \leq 0.5$ at 200A GeV, and $|\eta| \leq 0.8$ at 2.76A and 5.02A TeV.

From Fig. 5(a) we see that the improved AMPT model can reasonably reproduce the mid-pseudorapidity $dN_{ch}/d\eta$ data for the most central (0-5% centrality) collisions at all these energies except for 39A GeV and 62.4A GeV, where it underestimates the data. We also see that the model can reasonably describe the centrality dependence of $dN_{ch}/d\eta$ in Au+Au collisions at RHIC ener-

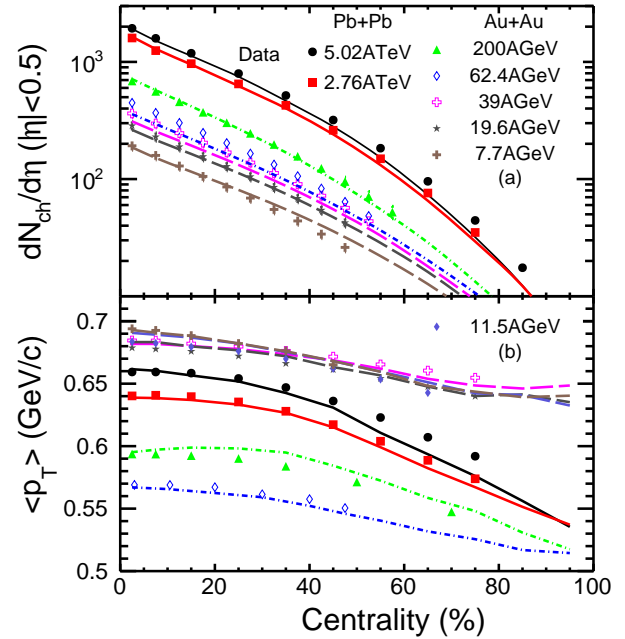


FIG. 5. $dN_{ch}/d\eta$ within $|\eta| < 0.5$ (a) and the mean transverse momentum $\langle p_T \rangle$ around mid-rapidity (b) versus centrality in Au+Au collisions at RHIC energies and Pb+Pb collisions at LHC energies from the AMPT model (curves) in comparison with the experimental data (symbols). Note the different p_T range used for the $\langle p_T \rangle$ calculation: $[0.15, 2]$ GeV/c (solid), $[0.2, 2]$ GeV/c (dot-dashed), $[0.4, 1.3]$ GeV/c (dashed).

gies [50], while for Pb+Pb collisions at 2.76A TeV [49] and 5.02A TeV [51] it underestimates the $dN_{ch}/d\eta$ for peripheral collisions. Figure 5(b) shows that the string melting version of the AMPT model describes the energy dependence of $\langle p_T \rangle$ reasonably well for Au+Au and Pb+Pb collisions over the colliding energies from 7.7A GeV to 5.02A TeV. The model underestimates the $\langle p_T \rangle$ for peripheral collisions at the LHC energies while overestimates the $\langle p_T \rangle$ for semi-peripheral and peripheral collisions at the top RHIC energy of 200A GeV; however, the difference from the data is no more than $\approx 3\%$.

We now compare this work with two earlier versions of the string melting AMPT model in Fig. 6(a) for $dN_{ch}/d\eta$ within $|\eta| < 0.5$ and in Fig. 6(b) for the $\langle p_T \rangle$ around mid-rapidity versus centrality in Pb+Pb collisions at 5.02A TeV and Au+Au collisions at 200A GeV. When we do not use the local nuclear scaling of p_0 and b_L but instead use constant $b_L = 0.15 \text{ GeV}^{-2}$ and a constant $p_0(s)$ at a given energy for the AMPT model of this work, the model is the same as the one developed in Ref. [31], and we obtain the dot-dashed curves when using $p_0(s) = p_0^{AA}(s)$ and the dotted curves when using $p_0(s) = p_0^{pp}(s)$ (note however that $p_0^{AA}(s) = p_0^{pp}(s)$ at 200A GeV). Results from the public AMPT version 2.26t9 [52] are also shown (dashed curves) for comparison, where the Lund parameters are

taken as $a_L = 0.55$ at 200A GeV and 0.30 at 5.02A TeV with $b_L = 0.15 \text{ GeV}^{-2}$ [20].

In Fig. 6(a) we see that the charged particle yield in central Pb+Pb collisions at 5.02A TeV from using $p_0(s) = p_0^{pp}(s)$ is much higher than the experimental data, and it is necessary to use the global nuclear scaling [31], i.e., $p_0(s) = p_0^{AA}(s)$, to reduce the total minijet cross section and consequently the particle yield. For peripheral collisions, however, the effect from the nuclear scaling of p_0 is much smaller because the binary scaling of minijet productions makes p_0 less important than for central collisions. These features are essentially the same as our earlier results (Fig. 11 of Ref. [22]). We also see as expected that the $dN_{\text{ch}}/d\eta$ results from this work are close to the AMPT results using the constant p_0^{AA} for central collisions but close to the AMPT results using the constant p_0^{pp} for peripheral collisions. In addition, we see that, compared to the $dN_{\text{ch}}/d\eta$ results from the AMPT version 2.26t9, results from this work are slightly worse at 5.02A TeV but slightly better at 200A GeV.

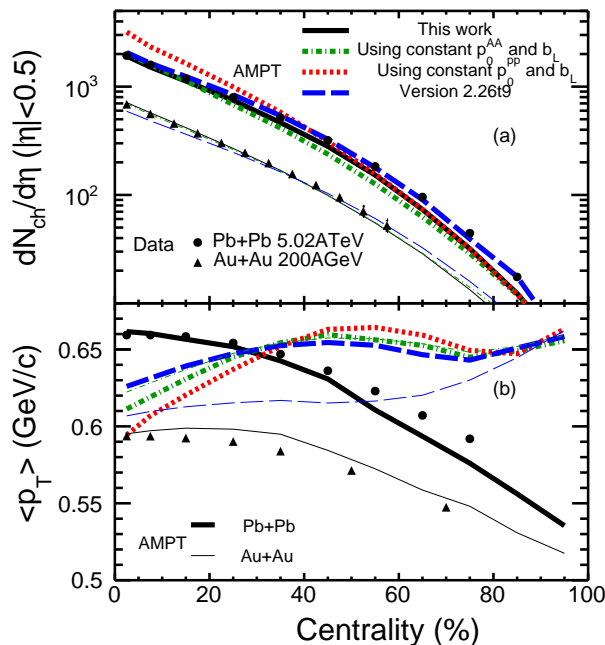


FIG. 6. $dN_{\text{ch}}/d\eta$ within $|\eta| < 0.5$ (a) and $\langle p_T \rangle$ around mid-pseudorapidity (b) versus centrality in 5.02A TeV Pb+Pb collisions (thick curves) and 200A GeV Au+Au collisions (thin curves) from this work (solid curves) and earlier versions of the AMPT model in comparison with the experimental data (symbols); the p_T range used for the $\langle p_T \rangle$ calculation is $[0.15, 2] \text{ GeV}/c$ at 5.02A TeV and $[0.2, 2] \text{ GeV}/c$ at 200A GeV.

Previously we found that the centrality dependence of charged particle $\langle p_T \rangle$ from the AMPT model is inconsistent with the experimental data at RHIC and LHC [26]. This is the case in Fig. 6(b) for the results from the AMPT version 2.26t9 (dashed curves). Simi-

larly, the AMPT model when using constant $b_L = 0.15 \text{ GeV}^{-2}$ and constant $p_0(s)$ (at a given energy) [31] gives the wrong centrality dependence of $\langle p_T \rangle$ around mid-pseudorapidity, where the model results (dot-dashed or dotted) show a mostly increasing trend with the increase of centrality while the data show a mostly decreasing trend. We also find that the decrease of $\langle p_T \rangle$ towards the most central events from both earlier AMPT versions (dotted, dashed, and dot-dashed curves) is mainly a result of the stronger parton rescatterings in more central collisions. On the other hand, the local nuclear scaling of this work enables the string melting AMPT model (solid curves) to reasonably reproduce the centrality dependence of charged particle $\langle p_T \rangle$ for the first time.

C. Smaller systems including $p\text{Pb}$ collisions

For the system size dependence, it is of particular interest to study the same observables in smaller systems like pA and other AA collisions. Figure 7 shows the results for three smaller collision systems: Xe+Xe collisions at 5.44A TeV [53, 54], Cu+Cu collisions at 200A GeV [50, 55], and $p\text{Pb}$ collisions at 5.02A TeV [56]. We use the same centrality estimator as the experiments, which is the charged particle multiplicity within $2.8 < \eta < 5.1$ and $-3.7 < \eta < -1.7$ for Xe+Xe collisions [54] and within $|\eta| < 3.2$ for Cu+Cu collisions [50]. For $p\text{Pb}$ collisions at 5.02A TeV, the experiment used the energy deposit in the ZDC detector coupled with a heuristic model related to the number of binary collisions (N_{coll}) to determine the centrality; due to the lack of slow nucleon physics in the AMPT model we use the model N_{coll} as the centrality estimator in the AMPT model calculations.

Figures 7(a) and 7(b) show respectively the mid-pseudorapidity $dN_{\text{ch}}/d\eta$ and $\langle p_T \rangle$ of charged particles from the AMPT model versus centrality in comparison with the experimental data for the three collision systems. The $\langle p_T \rangle$ values are calculated for hadrons around mid-pseudorapidity: $|\eta| < 0.8$ for XeXe collisions, $0.2 < \eta < 1.4$ for CuCu collisions, and $|\eta| < 0.3$ for $p\text{Pb}$ collisions. We see that the improved AMPT model describes these data rather well, confirming the validity of our method of using local nuclear scaling for the p_0 and b_L parameters. This is noteworthy because the data of these smaller systems are not considered in the fitting of the parameter functions such as $\alpha(s)$ and $\beta(s)$ in this study, although the mid-pseudorapidity $dN_{\text{ch}}/d\eta$ and $\langle p_T \rangle$ data for the most central Au+Au/Pb+Pb collisions have been used. Also note that the AMPT results in Fig. 7 underestimate both the mid-pseudorapidity $dN_{\text{ch}}/d\eta$ and $\langle p_T \rangle$ for peripheral Xe+Xe collisions; however, in this study we have not included the non-spherical deformation of the Xe nucleus [57].

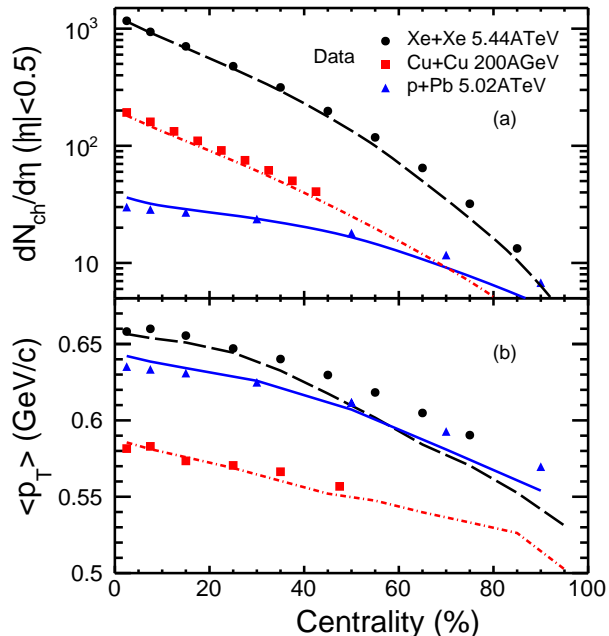


FIG. 7. $dN_{\text{ch}}/d\eta$ within $|\eta| < 0.5$ (a) and $\langle p_T \rangle$ around mid-pseudorapidity (b) versus centrality in Xe+Xe collisions at 5.44A TeV, Cu+Cu collisions at 200A GeV, and pPb collisions at 5.02A TeV from the AMPT model (curves) in comparison with the experimental data (symbols). The p_T range used for the $\langle p_T \rangle$ calculation is $[0.2, 2]$ GeV/c at 200A GeV and $[0.15, 2]$ GeV/c at the other two LHC energies.

IV. DISCUSSIONS

The local nuclear scalings of the b_L parameter in Eq.(3) and p_0 parameter in Eq.(7) both depend on the geometric mean of the two nuclear thickness functions, $\sqrt{T_A(s_A)T_B(s_B)}$; therefore, this geometric form of scaling is similar to the binary scaling in heavy ion collisions. On the other hand, one could also scale the two parameters according the arithmetic mean of the two thickness functions as the following:

$$b_L(s_A, s_B, s) = b_L^{pp} / \left[\frac{T_A(s_A) + T_B(s_B)}{2 T_p} \right]^{\beta(s)}, \quad (9)$$

$$p_0(s_A, s_B, s) = p_0^{pp}(s) * \left[\frac{T_A(s_A) + T_B(s_B)}{2 T_p} \right]^{\alpha(s)}, \quad (10)$$

and this arithmetic form of local scaling is similar to the participant scaling. For symmetric (AA) collision systems at impact parameter $b = 0$ fm, the two different forms are almost identical, because $T_A(s_A) = T_B(s_B)$ is approximately true which then reduces Eq. (9) to Eq.(3) and Eq. (10) to Eq.(7). Therefore, we expect that the different forms will not affect the model results for the most central AA collisions. On the other hand, the centrality

dependence and the system size dependence of observables could be different for the two different forms. One can expect from Eqs. (3), (7), (9) and (10) that the difference between the two forms will be the biggest for the most asymmetric collisions, i.e., central pA collisions.

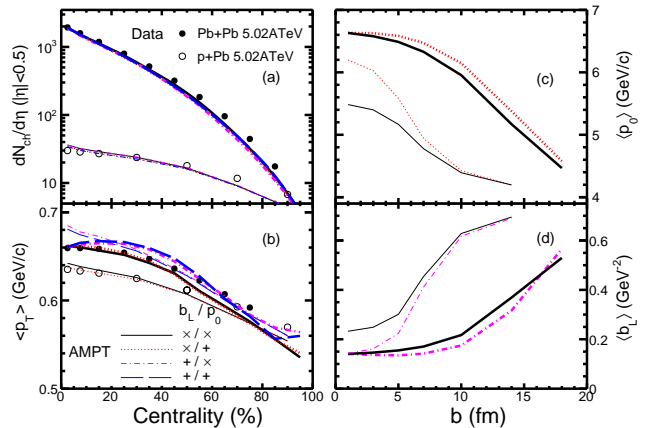


FIG. 8. $dN_{\text{ch}}/d\eta$ within $|\eta| < 0.5$ (a) and $\langle p_T \rangle$ around mid-pseudorapidity (b) versus centrality, as well as $\langle p_0 \rangle$ (c) and $\langle b_L \rangle$ (d) versus the impact parameter, for 5.02A TeV Pb+Pb (thick curves) and pPb collisions (thin curves) from different forms of local nuclear scaling in the AMPT model (see text for details); symbols represent the experimental data.

In Figs. 8(a) and 8(b) we compare the AMPT model results of $dN_{\text{ch}}/d\eta$ and $\langle p_T \rangle$ around mid-pseudorapidity versus centrality for both Pb+Pb and pPb collisions at 5.02A TeV. Since one can choose separate forms for the local nuclear scaling of b_L and p_0 , the model results including four different combinations, e.g., the curves labeled as “x/x” represent our default results of using the geometric form for both b_L and p_0 , while the curves labeled as “x/+” represent the model results of using the geometric form of Eq. (3) for b_L but the arithmetic form of Eq. (10) for p_0 . We see that different forms have a relatively small effect on the $dN_{\text{ch}}/d\eta$ yield and its centrality dependence. On the other hand, they have a significant effect on the mean transverse momentum, especially for pPb collisions, where the arithmetic form for the b_L scaling significantly over-predicts the experimental data, regardless of the form used for the p_0 scaling. Therefore, we choose the geometric form for the local scalings of both b_L and p_0 as shown in Eqs. (3) and (7), while we note that the arithmetic form for the scaling of p_0 would work similarly well as indicated by the dotted curves in Fig. 8. We note that a Bayesian analysis of the TRENTo initial condition [58] with a hybrid model found that the geometric form for the initial state entropy deposition is preferred by the experimental data than several other forms including the arithmetic form [59].

We show in Figs. 8(c) and 8(d) the impact parameter dependence of $\langle p_0 \rangle$ and $\langle b_L \rangle$, respectively, from the two different forms of local nuclear scaling. Indeed, the difference between the geometric and arithmetic forms is the

biggest for central p Pb collisions, where the arithmetic form gives a bigger variation of the $\langle p_0 \rangle$ and $\langle b_L \rangle$ values with the impact parameter. As a result, the higher p_0 value from the arithmetic form leads to a lower $dN_{\text{ch}}/d\eta$ while the lower b_L value from the arithmetic form gives a higher $\langle p_T \rangle$ for p Pb collisions.

V. SUMMARY

A multi-phase transport model can describe multiple observables in relativistic heavy ion collisions and can thus be very useful for the study of the dynamics and physical properties of the dense matter. However, certain key parameters need to have significantly different values for pp and central AA collisions for the model to well describe the yield and transverse momentum spectrum of the bulk matter. In this study we use local nuclear scaling to relate two key parameters in the initial condition to the nuclear thickness functions of the two colliding nuclei so that the parameter values change with the system size self consistently. Specifically, we let two parameters in the string melting AMPT model with modern parton distribution functions of nuclei, the Lund string fragmentation parameter b_L and the minijet transverse momentum cutoff p_0 , to scale with powers of $\sqrt{T_A(s_A)T_B(s_B)}$ similar to the number of binary collisions. We then systematically study charged particle productions in different collision systems over a wide energy range.

We start from the parameter values for pp collisions that allow a good description of the charged particle yields and transverse momentum spectra in pp collisions

from 23.6 GeV to 13 TeV. We then determine the two energy-dependent power functions in the local nuclear scaling of the p_0 and b_L parameters by comparing to data on the charged particle $dN_{\text{ch}}/d\eta$ and mean transverse momentum $\langle p_T \rangle$ (below $p_T \lesssim 2$ GeV) around mid-pseudorapidity in the most central Au+Au and Pb+Pb collisions. Then the centrality dependence and system size dependence are model predictions. We show that, for charged particles around mid-pseudorapidity in Au+Au collisions from 7.7A GeV to 200A GeV and Pb+Pb collisions at LHC energies, the improved AMPT model not only provides reasonable descriptions of the centrality dependence of the $dN_{\text{ch}}/d\eta$ yield but also for the first time well describes the centrality dependence of $\langle p_T \rangle$. The model also provides reasonable descriptions of smaller systems including p Pb, Cu+Cu and Xe+Xe collisions without any change of the parameter functions. This work allows a multi-phase transport model to describe the system size and centrality dependences of nuclear collisions self consistently, making the model more reliable for further studies of nuclear collisions from small to large systems.

ACKNOWLEDGMENTS

This work is supported by the National Natural Science Foundation of China under Grants No. 11890711 (C.Z. and S.S.S.) and No. 11905188 (L.Z.), the National Key Research and Development Program of China under Grant No. 2020YFE0202002 (C.Z. and S.S.S.), the Chinese Scholarship Council (C.Z.), and the National Science Foundation under Grant No. 2012947 (Z.-W.L.).

-
- [1] S. A. Bass *et al.* Prog. Part. Nucl. Phys. **41**, 255-369 (1998).
 - [2] Z. Xu and C. Greiner, Phys. Rev. C **71**, 064901 (2005).
 - [3] Z. W. Lin, C. M. Ko, B. A. Li, B. Zhang and S. Pal, Phys. Rev. C **72**, 064901 (2005).
 - [4] W. Cassing and E. L. Bratkovskaya, Nucl. Phys. A **831**, 215-242 (2009).
 - [5] P. Huovinen, P. F. Kolb, U. W. Heinz, P. V. Ruuskanen and S. A. Voloshin, Phys. Lett. B **503**, 58-64 (2001).
 - [6] B. Betz, J. Noronha, G. Torrieri, M. Gyulassy, I. Mishustin and D. H. Rischke, Phys. Rev. C **79**, 034902 (2009).
 - [7] B. Schenke, S. Jeon and C. Gale, Phys. Rev. Lett. **106**, 042301 (2011).
 - [8] P. Bozek, Phys. Rev. C **85**, 014911 (2012).
 - [9] H. Petersen, J. Steinheimer, G. Burau, M. Bleicher and H. Stöcker, Phys. Rev. C **78**, 044901 (2008).
 - [10] K. Werner, I. Karpenko, T. Pierog, M. Bleicher and K. Mikhailov, Phys. Rev. C **82**, 044904 (2010).
 - [11] H. Song, S. A. Bass, U. Heinz, T. Hirano and C. Shen, Phys. Rev. Lett. **106**, 192301 (2011). [erratum: Phys. Rev. Lett. **109**, 139904 (2012)].
 - [12] K. Dusling, M. Mace and R. Venugopalan, Phys. Rev. Lett. **120**, 042002 (2018).
 - [13] M. Mace, V. V. Skokov, P. Tribedy and R. Venugopalan, Phys. Rev. Lett. **121**, 052301 (2018) [erratum: Phys. Rev. Lett. **123**, 039901 (2019)].
 - [14] L. He, T. Edmonds, Z. W. Lin, F. Liu, D. Molnar and F. Wang, Phys. Lett. B **753**, 506-510 (2016).
 - [15] Z. W. Lin, L. He, T. Edmonds, F. Liu, D. Molnar and F. Wang, Nucl. Phys. A **956**, 316-319 (2016).
 - [16] R. D. Weller and P. Romatschke, Phys. Lett. B **774**, 351-356 (2017).
 - [17] A. Kurkela, U. A. Wiedemann and B. Wu, Phys. Lett. B **783**, 274-279 (2018).
 - [18] A. Kurkela, U. A. Wiedemann and B. Wu, Eur. Phys. J. C **79**, 965 (2019).
 - [19] X. N. Wang and M. Gyulassy, Phys. Rev. D **44**, 3501-3516 (1991).
 - [20] Z. W. Lin, Phys. Rev. C **90**, 014904 (2014).
 - [21] Y. He and Z. W. Lin, Phys. Rev. C **96**, 014910 (2017).
 - [22] C. Zhang, L. Zheng, F. Liu, S. Shi and Z. W. Lin, Phys. Rev. C **99**, 064906 (2019).
 - [23] B. Andersson, G. Gustafson and B. Soderberg, Z. Phys. C **20**, 317 (1983).
 - [24] B. Andersson, G. Gustafson, G. Ingelman and T. Sjostrand, Phys. Rept. **97**, 31-145 (1983).
 - [25] T. Sjostrand, Comput. Phys. Commun. **82**, 74-90 (1994).
 - [26] G. L. Ma and Z. W. Lin, Phys. Rev. C **93**, 054911 (2016).

- [27] K. J. Eskola, V. J. Kolhinen and P. V. Ruuskanen, Nucl. Phys. B **535**, 351-371 (1998).
- [28] E. Eichten, I. Hinchliffe, K. D. Lane and C. Quigg, Rev. Mod. Phys. **56**, 579-707 (1984).
- [29] W. T. Deng, X. N. Wang and R. Xu, Phys. Rev. C **83**, 014915 (2011).
- [30] L. D. McLerran and R. Venugopalan, Phys. Rev. D **49**, 2233-2241 (1994).
- [31] L. Zheng, C. Zhang, S. S. Shi and Z. W. Lin, Phys. Rev. C **101**, 034905 (2020).
- [32] W. Thome *et al.* [Aachen-CERN-Heidelberg-Munich Collaboration], Nucl. Phys. B **129**, 365 (1977).
- [33] A. Adare *et al.* [PHENIX Collaboration], Phys. Rev. C **83**, 064903 (2011).
- [34] J. Adams *et al.* [STAR Collaboration], Phys. Rev. Lett. **91**, 172302 (2003).
- [35] C. Albajar *et al.* [UA1 Collaboration], Nucl. Phys. B **335**, 261-287 (1990).
- [36] C. Roland, CMS-CR-2010-056, contribution to 45th Rencontres de Moriond on QCD and High Energy Interactions, 47-50.
- [37] F. Abe *et al.* [CDF Collaboration], Phys. Rev. D **41**, 2330 (1990).
- [38] B. B. Abelev *et al.* [ALICE Collaboration], Eur. Phys. J. C **73**, 2662 (2013).
- [39] S. Acharya *et al.* [ALICE Collaboration], JHEP **11**, 013 (2018).
- [40] V. Khachatryan *et al.* [CMS Collaboration], Phys. Rev. Lett. **105**, 022002 (2010).
- [41] J. Adam *et al.* [ALICE Collaboration], Phys. Lett. B **753**, 319-329 (2016).
- [42] T. Sjostrand, S. Mrenna and P. Z. Skands, JHEP **05**, 026 (2006).
- [43] J. Adam *et al.* [ALICE Collaboration], Eur. Phys. J. C **77**, 33 (2017).
- [44] G. J. Alner *et al.* [UA5 Collaboration], Z. Phys. C **33**, 1-6 (1986).
- [45] B. Alper *et al.* [British-Scandinavian ISR Collaboration], Phys. Lett. B **44**, 521-526 (1973).
- [46] F. Abe *et al.* [CDF Collaboration], Phys. Rev. Lett. **61**, 1819 (1988).
- [47] L. Adamczyk *et al.* [STAR Collaboration], Phys. Rev. C **96**, 044904 (2017).
- [48] B. B. Back *et al.* [PHOBOS Collaboration], Phys. Rev. Lett. **94**, 082304 (2005).
- [49] B. Abelev *et al.* [ALICE Collaboration], Phys. Lett. B **720**, 52-62 (2013).
- [50] A. Adare *et al.* [PHENIX Collaboration], Phys. Rev. C **93**, 024901 (2016).
- [51] J. Adam *et al.* [ALICE Collaboration], Phys. Lett. B **772**, 567-577 (2017).
- [52] Source codes of various AMPT versions are available at <http://myweb.ecu.edu/linz/ampt/>
- [53] S. Acharya *et al.* [ALICE Collaboration], Phys. Lett. B **788**, 166-179 (2019).
- [54] S. Acharya *et al.* [ALICE Collaboration], Phys. Lett. B **790**, 35-48 (2019).
- [55] B. Alver *et al.* [PHOBOS Collaboration], Phys. Rev. Lett. **96**, 212301 (2006).
- [56] J. Adam *et al.* [ALICE Collaboration], Phys. Rev. C **91**, 064905 (2015).
- [57] P. Möller, A. J. Sierk, T. Ichikawa and H. Sagawa, Atom. Data Nucl. Data Tabl. **109-110**, 1-204 (2016).
- [58] J. S. Moreland, J. E. Bernhard and S. A. Bass, Phys. Rev. C **92**, 011901 (2015).
- [59] J. E. Bernhard, J. S. Moreland, S. A. Bass, J. Liu and U. Heinz, Phys. Rev. C **94**, 024907 (2016).